Front. Phys. 13(5), 137309 (2018)
https://doi.org/10.1007/s11467-018-0815-x

RESEARCH ARTICLE

Alkali-metal-induced topological nodal line semimetal in layered XN_2 (X = Cr, Mo, W)

Ali Ebrahimian[†], Mehrdad Dadsetani[‡]

Department of Physics, Lorestan University, Khoramabad, Iran
E-mail: [†]ebrahimian.Al@fs.lu.ac.ir, [‡]dadsetani.m@lu.ac.ir
Received April 19, 2018; accepted June 2, 2018

Based on first principles calculations and the $\boldsymbol{K}\cdot\boldsymbol{p}$ effective model, we propose that alkali metal deposition on the surface of hexagonal XN_2 (X = Cr, Mo, W) nanosheets induces topologically nontrivial phases in these systems. When spin orbit coupling (SOC) is disregarded, the electron-like conduction band from N-p_z orbitals can be considered to cross the hole-like valence band from X-d_z^2 orbitals, thereby giving rise to a topological nodal line state in lithium-functionalized XN_2 sheets (Li_2MoN_2 and Li_2WN_2). Such band crossing is protected by the existence of mirror reflection and time reversal symmetry. More interestingly, the bands cross exactly at the Fermi level, and the linear dispersion regions of such band crossings extend to as high as 0.9 eV above the crossing. For Li_2CrN_2, the results reveal the emergence of a Dirac cone at the Fermi level. Our calculations show that lattice compression decreases the thickness of a Li_2CrN_2 nanosheet, leading to phase transition to a nodal line semimetal. The evolution of the band gap of Li_2XN_2 at the Γ point indicates that the nontrivial topological character of Li_2XN_2 nanolayers is stable over a large strain range. When SOC is included, the band crossing point is gapped out giving rise to quantum spin Hall states in Li_2CrN_2 nanosheets, while for Li_2MoN_2, the SOC-induced gap at the crossing points is negligible.

Keywords topological semimetal, nodal-line states, Dirac cone, band inversion

PACS numbers 73.20.-r, 71.55.Ak, 73.20.At

1 Introduction

With the discovery of topological insulators [1–5], topological phases of matter have become the most active topic in condensed matter physics and there has been a tremendous amount of research in the search for novel topological materials, resulting in the realisation of new topological phases of matter such as topological semimetals [6–8]. In toplogical semimetals, the band inversion gives rise to a linear crossing in the bulk which can be in the form of zero-dimensional (0D) nodal points or a one-dimensional (1D) nodal ring (or nodal lines) [9–14]. The low-energy excitations of these symmetry protected band crossings are linearly dispersing Weyl or Dirac fermions [15–18]. The digeneracy and dimensionality of the band touching can be used to classify topological semimetals into Dirac semimetals [19], Weyl semimetals [20, 21] and nodal line semimetals [22]. Dirac and Weyl semimetals have 0D band crossing points while in nodal line semimetals the band touching points form a closed ring in momentum space. The band touching points behave as the sources or sinks of Berry curvature and have topologically protected charges [23].

The topological invariant of the band touching points can be identified based on the line integral of Berry connection along any closed loop that surronds a nodal point or threads the nodal line [23–26]. So far many materials have been predicted to be 3D toplogical semimetals [26–28] and some of them have been experimentally verified in angle-resolved photoelectron spectroscopy(ARPES) studies [29–36]. Research on topological semimetals reveals their exotic properties such as high charge carrier mobility [37, 38], large magnetoresistance [37] and potential topological superconductivity [39–42]. Furthermore, 3D nodal line semimetals with high energy range of the linearly dispersed bands and high Dirac fermion densities enhance our knowledge of topological semimetals [43, 44]. After the comprehensive understanding of 3D topological semimetals, considerable attention is now focused on 2D topological nodal line semimetals. Graphene as a first experimentally synthesized 2D material hosts Dirac

points at the Fermi level in the presence of weak spin-orbit coupling (SOC) and inversion symmetry. In fact 2D toplogical semimetals are fragile and are more challenging to be captured in real materials. However, Young and Kane have shown the possibility for the existence of 2D topological semimetals that host symmetry-protected 2D Dirac points in the presence of SOC [45].

Nodal line semimetals have been predicted to exsit in two-dimensional compounds X_2Y (X = Ca, Sr and Y = As, Sb, Bi) [46], honeycomb-kagome lattices [47], monolayer transition-metal group VI compounds [48], two dimensional Lieb lattices [49] and surface-functionalized XN_2 sheets (X = Mo, W) [50]. Recently Feng et al. have imaged Dirac nodal loops in monolayer Cu_2Si by ARPES [51]. However, this expanding class of topological semimetals is still under development and the preparation of new 2D nodal line semimetals with novel properties such as linear dispersion of the Dirac cone and nearly flat surface states [46] offers a route to improve our knowledge of Dirac and Weyl fermions, high-speed nano devices and high-temperature super conductivity [52]. Among two-dimensional materials, transition-metal dichalcogenides (TMDCs) are particularly appealing due to their potential for future nanoelectronics applications, such as spintronics and valleytronics devices [53, 54]. Recently a stable class of 2D TMDCs of composition MX_2 (M = Mo, W; X = S, Se, Te) with hexagonal lattice have been proposed as large band gap topological insulators [55, 56]. Furthermore, ab inito calculations show that surface termination can induce a Quantum spin Hall (QSH) insulator state in XN_2 (X = Mo, W) nanolayers, having structure similar to hexagonal MX_2 [57]. More excitingly, experimental and theoretical results show that adsorption of alkali metals on TMDCs results in 2D conduction channels (Quantum well states) and a nearly free 2D electron gas providing access to the conduction band [58, 59].

Our previous calculations show that that adsorption of alkali metal induces topological semimetals in 2D nanosheets [50]. Motivated by these results, we suggest here that adsorption of alkali metals can be a route for creating topological semimetals in hexagonal XN_2 nanossheet. We have used density functional theory (DFT) and the $\boldsymbol{K}\cdot\boldsymbol{p}$ model to investigate the effect of adsorption of alkali metal atom (Li) on the band stucture and electronic properties of hexagonal XN_2 (X = Cr, Mo, W) and explored the possible existence of topological phases in these 2D materials. Our results show that alkali metal atom (Li) deposition on the surface of XN_2 (Cr, Mo, W) nanosheets causes the appearance of a parabolic conduction band near the Fermi level with noticeable down-shift from CrN_2 to MoN_2, resulting in the realisation of a nodal line semimetal in a Li_2MoN_2 (Li_2WN_2) nanolayer. In other words, we demonstrate that a Li_2CrN_2 nanosheet hosts QSH states with an energy gap of 17.5 meV while Li_2MoN_2 (Li_2WN_2) is a new topological nodal line semimetal with a Dirac cone at Fermi level. The band inversion, which is a crucial sign of the nontrivial band topology is observed between the X-d orbitals and the N-p_z orbital due to the crystal field effect. The results strongly discourage the use of different exchange-correlation functional approximations. Indeed, to avoid the underestimation of the fundamental gap, we have checked the band crossing by using the hybrid functional HSE06 [60, 61] as well as the modified Becke-Johnson (mBJ) functional [62]. More interestingly, the linear dispersion regions of band crossings extend to as high as 0.9 eV above the crossing, making Li_2MoN_2 (Mo, W) an ideal platform to study Dirac and Weyl physics as well as device design based on 2D topological semimetals. Our results suggest a new route to design topological semimetals and an ideal platform to investigate their exotic properties. Due to the common features shared by Li_2MoN_2 and Li_2WN_2, we will focous in this work mainly on the topological properties of Li_2MoN_2 and Li_2CrN_2. In Section 2 we introduce briefly the calculation methods. Section 3 is devoted to the results of the study, focusing on the structural and electronic properties of surface functionalized hexagonal XN_2 (Cr, Mo, W). Finally we summarise our results and present some concluding remarks.

2 Calculation method

For high accuracy electronic structure calculations, the structural optimization and electronic properties are modeled by using the all-electron full potential linearized augmented plane wave (FP-LAPW) method as implemented in the WIEN2k code [63] and the FHI-aims code package, the latter of which is an all-electron full potential electronic structure code including numerical atom-centered orbitals [64]. The generalized gradient approximation of Perdew–Burke–Ernzerhof (PBE) is used for the exchange-correlation potential [65]. The $\boldsymbol{k}$-point sampling grid in the electronic calculations was $20 \times 20 \times 1$. For each configuration, the atomic positions and lattice parameters are optimized until the maximum residual force on each atom becomes less than 10^{-4} eV/Å. The SOC is included self-consistently within the second-variational method. A 18 Å thick vacuum layer is used to avoid interactions between nearest layers. It is well known that generalized gradient approximation (GGA) functionals systematically underestimate the band gap. Therefore, to avoid the possible underestimation of the band gap within PBE functional, we have also employed the hybrid density functional (HSE06) [60, 61] and the mBJ potential [62].

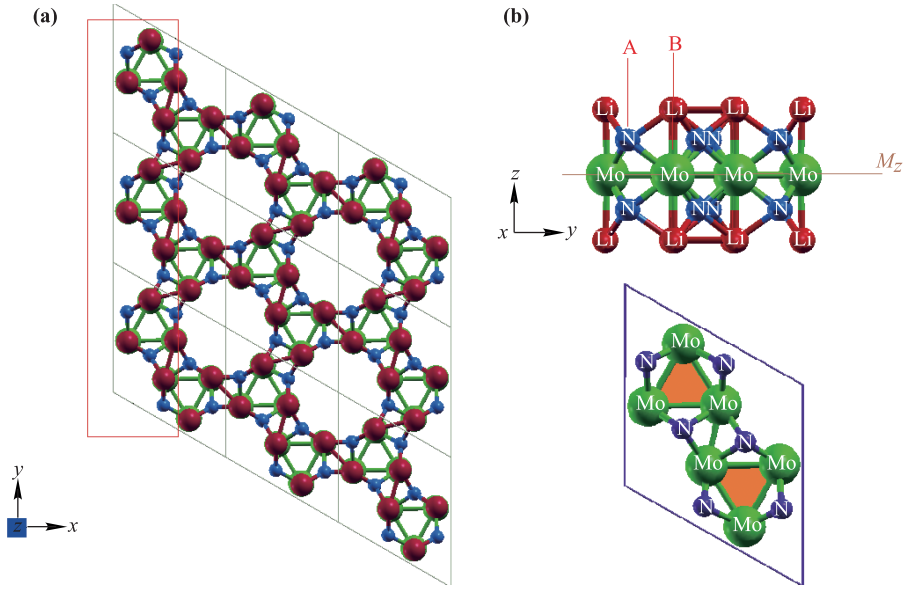

Fig. 1 **(a)** Top view of the crystal structure of Li_2MoN_2 (red line shows an armchair edge). **(b)** The possible sites (upper panel) for surface termination are A (on top of the N site) and B (on the top of Mo site). The mirror reflection plane is shown by M_z. Top view (lower panel) of the crystal structure of MoN_2.

3 Results and discussion

3.1 Structural properties

We first characterize the crystal structure of hexagonal XN_2 (Cr, Mo, W) nanolayers. The nansheet XN_2 has a similar structure to MoS_2 [55, 56] which is composed of repeated MoS_2 square and hexagon units. It crystallizes in hexagonal space group P6/m (No. 175) and each unit cell contains 6 transition metal (Cr, Mo, W) and 12 Nitrogen (N) atoms (Fig. 1). In XN_2 nannsheet, transition metal atoms make a plane sandwiched between two N atomic layer. Liu *et al.* have shown that hydrogenation could enhance the structural stability of XN_2 (Mo, W) [57]. Their calculation shows that Hydrogen (H) atoms are located on top of the N atoms to make layering sequence of H-N-X-N-H. These structures host QSH states due to band inversion between X-$d_{xy}/d_{x^2-y^2}$ and X-d_z^2 bands. To explore the effects of alkali metal on the structural properties of XN_2, the bare surfaces of XN_2 nanosheet are terminated by Lithium (Li) atoms. As shown in Fig. 1, there are two possible adsorption sites on each surface, namely A and B. In fact, Li atoms can be located on the top of the N atoms (A) or on the top of the X (Cr, Mo, W) atoms (B). For each case, the crystal structure of Li_2XN_2 is fully optimized and its total energy is calculated. Our calculations show that the B-site Lithium-functionalization of XN_2 obtains the lowest energy and is more stable than the A-site. Figure 1 show that Li atoms on the top of the X atoms bound to nearest N atoms to make a ring, causing reduction in total energy. The decorated atoms pull out the N atoms which results in larger thickness for XN_2 layer. Compared to H_2XN_2 sheet, the Li_2XN_2 has larger thickness. Interestingly, we note that this structure (XN_2) resembles the structure of a mixed lattice composed by Kagome and honey comb lattices such as Hg_3As_2 which has been recently proposed as 2D nodal line semimetal [47]. By replacing As (Hg) atoms with a triangle of X atoms (dimer of N atoms), the structure of XN_2 can be obtained (Fig. 1). In order to check the structural stability of Li_2XN_2 nanosheets, we calculated a set of phonon dispersions. As Fig. 2 shows, all branches over the entire Brillouin zone have positive frequencies, indicating that these structures are dynamically stable. The highest phonon frequency in Li_2XN_2 is around 700 cm^{-1} which is higher than that for MoS_2 475 cm^{-1} [66].

3.2 Electronic structure

After describing the lattice structure of Li_2XN_2 nanolayers, we turn to investigate their electronic and topological properties. Since the band structures of Li_2MoN_2 and Li_2WN_2 are qualitatively the same, the electronic band structures of Li_2MoN_2 and Li_2CrN_2 are shown in

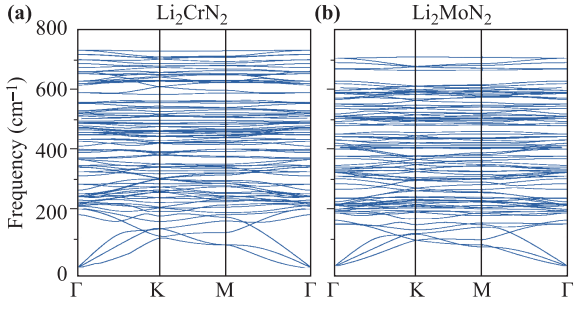

Fig. 2 The phonon dispersions for optimized Li_2CrN_2 **(a)** and Li_2MoN_2 **(b)** nanosheets.

Fig. 3. The results for Li_2WN_2 are given in the Supplemental Material [67]. As shown in Fig. 3, when SOC is not considered, the topmost valence band and the lowest conduction band of Li_2CrN_2 touch at the Γ point around which the valence and conduction bands are both parabolic. This shows that Li_2CrN_2 is semimetallic. For the Li_2MoN_2 nanosheet, the valence and conduction bands cross each other at Femi level, making a nodal ring around the Γ point. The projected band structures onto the d orbitals of the X (Cr, Mo) atoms and the p orbitals of the N atoms are shown in Fig. 4.

Due to the existence of point group C_{6h} at the Γ point, the d orbitals are categorized into three groups $(d_{xy}, d_{x^2-y^2})$, (d_{xz}, d_{yz}) and d_z^2. Similarly, the p orbitals are split into two group (p_x, p_y) and p_z. The orbital-character analysis and projected partial densities of states show that the bands near Fermi level are composed mostly of X-d orbitals and N-p_z orbital. For Li_2CrN_2, the degenerate bands at Fermi level mainly composed of X-d_z^2 orbital. Above these degenerate states at the Γ point, there is a parabolic band from N-p_z orbital centered at Γ point. The next conduction band at the Γ point is mainly contributed by the X-$d_{xy}/d_{x^2-y^2}$ orbitals as shown by the band projections in Fig. 4. For the Li_2MoN_2 nanosheet, the electron-like conduction bands from the N-p_z orbitals cross the hole-like valence band from the Mo-d_z^2 orbital at Fermi level. In comparison to Li_2CrN_2, the state of N-p_z orbital shifts downward the Fermi energy while the states of Mo-d_z^2 orbital move above Fermi level with a 343 meV inversion gap. The stacking sequence of X, N and Li atomic planes within the unit cell is Li-N-X-N-Li which preserves space inversion symmetry. Therefore, the X atomic plane is a mirror plane of the structure under mirror operation R_z that

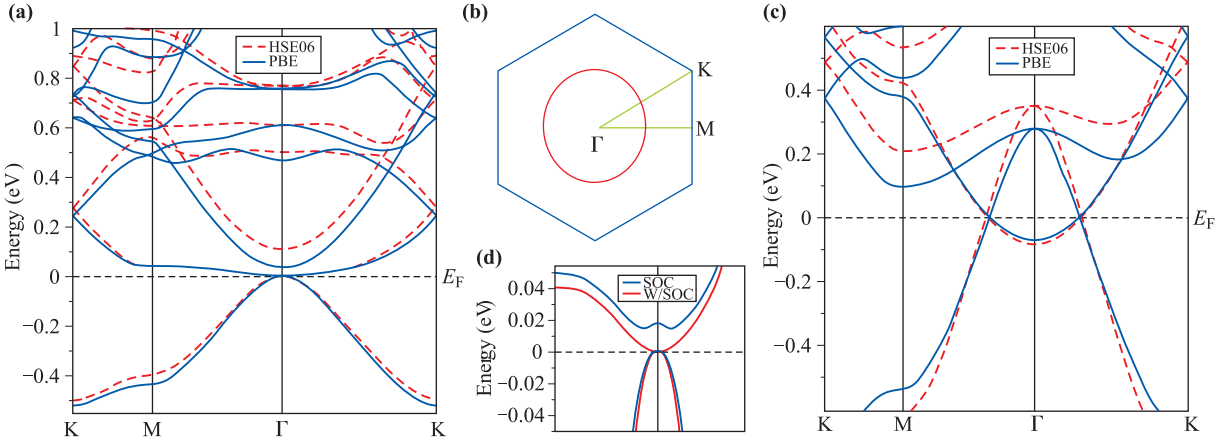

Fig. 3 The band structure of Li_2CrN_2 **(a)** and Li_2MoN_2 **(c)** calculated without spin-orbit coupling (SOC). **(b)** Momentum distribution of the nodal loop at the Fermi level in Li_2MoN_2. **(d)** The band structure of Li_2CrN_2 with/without SOC.

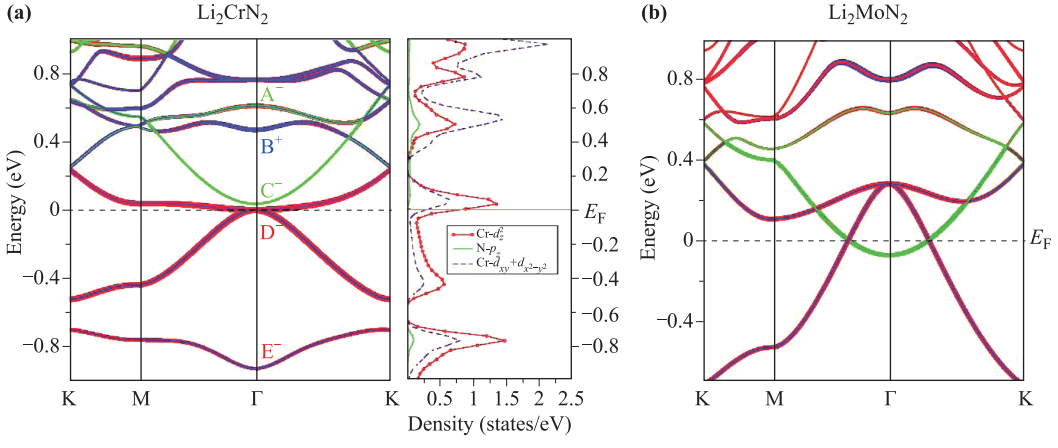

Fig. 4 The orbital-projected band structures and density of states of Li_2CrN_2 **(a)** and Li_2MoN_2 **(b)** into the X-d_z^2 (red line), N-p_z (green line) and X-$d_{xy}/d_{x^2-y^2}$ (blue line) orbitals where "+" and "−" represent the even and odd parity eigenvalues, respectively.

changes z to $-z$. Because of this in-plane mirror symmetry, the structure has C_s point group along Γ-M and Γ-K, which has two one-dimensional irreducible representations: A' and A''. The inverted two bands along Γ-M and Γ-K belong to different irreducible representations. The band constructed from X-d_z^2 belong to $\Gamma_2(A'')$ while the band constructed from N-p_z belong to $\Gamma_1(A')$. Therefore, the intersection of the two bands is protected by mirror reflection symmetry, making a continuous closed loop on the mirror plane $k_z = 0$ [68]. We have calculated the Fermi surface to consider the momentum distribution of gapless nodal points in the Brillouin zone. As Fig. 3 (part b) shows, the inverted bands form a node-line loop due to band crossing at Fermi level.

It is noteworthy that the two bands crossing the Fermi level have the same parity so the band crossing does not lead to a parity exchange between the occupied and unoccupied bands at the Γ point. We have checked the electronic structures by using the hybrid functional HSE06 [60, 61] as well as the modified Becke-Johnson (mBJ) functional [62]. Our results show that they give a similar band gap (Fig. 3).

In order to determine the accuracy of DFT results, we use the effective $\boldsymbol{K}\cdot\boldsymbol{p}$ Hamiltonian near the band inversion to check the existence of nodal line structure around the Γ point; see Supplemental Materials [67] for details. The result indicates that the band crossing in 2D momentum space forms a closed loop, which is in good agreement with the first-principles result. Motivated by the existence of the quantum spin Hall (QSH) effect in H_2XN_2 (Mo, W), we have calculated the z_2 topological invariant (υ) of Li_2XN_2 (Mo, Cr, W) nanolayers. Since the Li_2XN_2 nanolayers have the inversion symmetry, its z_2 topological invariant can be simply calculated by evaluating the parity eigenvalues of occupied states at time reversal-invariant momentum (TRIM) points of the Brillouin zone [69, 70]. Following the method proposed by Fu and Kane [69, 70], topological invariant υ is evaluated as

$$\delta(k_i) = \prod_{n=1}^{N} \xi_n(k_i),$$

$$(-1)^{\upsilon} = \prod_{i=1}^{4} \delta(k_i),$$

where $\xi_n(k_i)$ is $+1$ (-1) for even (odd) parity of the nth occupied band at time-reversal invariant momentum k_i and N is the total number of occupied bands. The topological invariant $\upsilon = 1$ $(\upsilon = 0)$ corresponds to nontrivial (trivial) topological phase. Hexagonal monolayer Li_2XN_2 has one TRIM point at $\Gamma(0,0)$ and three TRIM points at M_1 $(0, 0.5)$, M_2 $(0.5, 0)$ and M_3 $(0.5, 0.5)$ which have the same parities. The parity analysis of the occupied bands at TRIM points shows that the z_2 topological invariant υ is 1, indicating the nontrivial topological phase.

As shown in Fig. 3, upon considering the SOC, for Li_2CrN_2, the degeneracy of the topmost valence band and the lowest conduction band at Fermi level is lifted, introducing a finite energy gap of 17.5 meV and the system becomes a topological insulator. Figure 3 shows the SOC-induced W-shaped conduction band, which is a sign of a nontrivial phase. The SOC opens a band gap approximately 7.3 (22) meV along nodal line of Li_2MoN_2 (Li_2WN_2) which is negligible and smaller than the SOC-induced gap opening in the most reported nodal line semimetals [39].

Another remarkable feature of nontrivial topological phases is the emergence of topological edge states. To calculate the edge states of Li_2CrN_2 (Li_2MoN_2), we have constructed a nanoribbon with an armchair edge with approximately 51 (53) Å width to minimize the interaction between two edges of nanoribbons. As Fig. 5 shows, there is a nearly flat surface (red line) within the bulk band gap of Li_2MoN_2 which is a common feature of nodal line semimetals and have been reported for 2D nodal line Ca_2As [46]. For Li_2CrN_2, the emergent edge states (red lines) connect the conduction and valence bands to form a single Dirac cone at Γ point.

3.3 Band inversion mechanism

As illustrated before, for Li_2CrN_2, the SOC just opens a tiny gap at Γ point without any band inversion, implying that the band inversion has occurred before turning on SOC. To get insight into physical mechanism for band inversion, we take Li_2CrN_2 as an example and change the distance between neighboring atoms while analyzing the band order associated with atomic orbitals. In the stable structure of H_2XN_2 (X = Mo, W), H atoms are located on the top of N atoms [57]. So the band composed of N-p_z orbital is located at N-H bond (along vertical direction

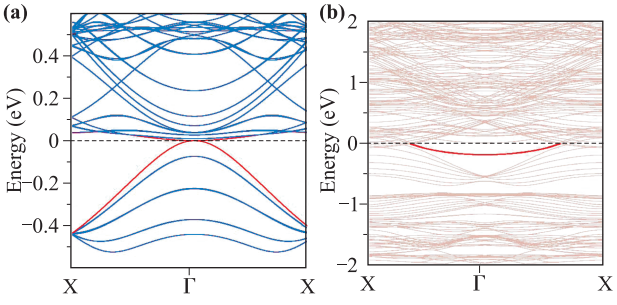

Fig. 5 Energy and momentum-dependent local density of states for Li_2XN_2 (X = Cr, Mo) on the armchair edge. **(a)** For Li_2CrN_2, the edge states (red line) that connect the bulk valence and conduction band edges form a single Dirac cone at the Γ point. **(b)** The nearly flat surface band (red line) is nestled within the projected bulk band structure (brown line) in Li_2MoN_2. The Fermi energy is located at zero energy.

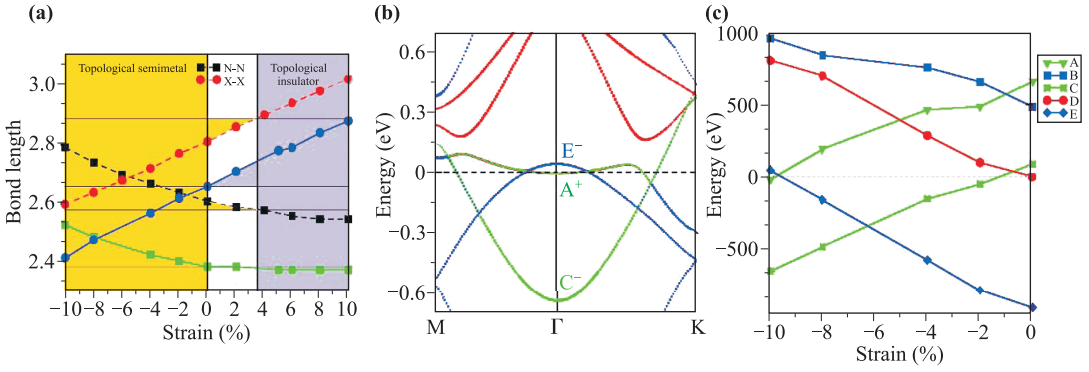

Fig. 6 **(a)** The evolution of N-N and X-X (X = Cr, Mo) distances in Li_2CrN_2 (solid line) and Li_2MoN_2 (dashed line) under lattice strain. **(b)** The orbital-projected band structure for −10% strained Li_2CrN_2 into the X-d_z^2 (red line), N-p_z (green line) and X-$d_{xy}/d_{x^2-y^2}$ (blue line) orbitals. **(c)** The evolution of closest bands to the Fermi level under lattice strain for Li_2CrN_2.

to the nanosheet) and does not contribute to bands near the Fermi level. For Li_2CrN_2, Li atoms are located on the top of Cr atoms, leading to overlap between Cr-d_z^2 and N-p_z orbitals near the Fermi level. As a result, the energy bands near Fermi level are from the bonding interactions between the Cr-d_{xy/x^2-y^2}, Cr-d_z^2 and N-p_z orbitals and are sensitive to variations of Cr-Cr and N-Cr distances (thickness of nanosheet). Our calculations show that N-p_z orbitals mostly contribute to two bands above Fermi level (labelled A, C). Other bands near the Fermi energy (labelled B, D and E) are composed from Cr-d_{xy/x^2-y^2} and Cr-d_z^2 orbitals (see Fig. 4). The double degenerate states of d_z^2 orbitals at Γ point are odd and split to two states with different parities (labeled + and −) by band dispersion along Γ-M, resulting "−" and "+" for the parity products of occupied states at M and Γ point respectively. The evolution of energy levels of band near to Fermi energy and X-X (N-N) bond length under lattice strain is depicted in Fig. 6. As the compressive strain is increased, the vertical distance between two N layers (the distance between X atoms) is increased (decreased). Therefore, the interaction between N-N atoms and hybridization between N-p_z and Cr-d_z^2 orbitals (Cr-d_z^2 and Cr-d_{xy/x^2-y^2}) will be weakened (enhanced); which lowers (raises) the energy of two bands A and C (B, D and E). By compressing the lattice constant $\boldsymbol{a}$ (Fig. 6), the band C (D) shift down (up) the Fermi level and the first band inversion happens at strain of about −1%, which does not change the parity products of occupied states at Γ point. This band inversion causes the phase transition from a QSH state to nodal line semimetal in Li_2CrN_2. When further compressing the lattice, the second band inversion happens between A and E which leads to parity exchange the occupied and unoccupied bands, including a topological semimetal to trivial insulator phase in Li_2CrN_2 at strain of about −9.5% (see Fig. 6).

4 Strain effects

Now we focus on the role of strain on the topological properties of a Li_2XN_2 monolayer. To explore the possibility of a topological phase transition, we have calculated the direct band gap at Γ as a function of lattice strain. To do so, the lattice constant $\boldsymbol{a}$ is compressed or extend and for each fixed volume, the internal atomic coordinates are fully optimized. As mentioned before the applied strain modifies the interaction between N-p_z, X-d_{xy/x^2-y^2} and X-d_z^2 orbitals, changing the energies of bands near to Fermi level. The calculation results are shown in Fig. 7. For Li_2CrN_2, when decreasing the lattice constant, the band composed of N-p_z orbital shift downward below the Fermi level and crosses X-d_z^2 band, making a nodal ring. In other words, lattice compression decreases the thickness of nanosheet, leading to phase

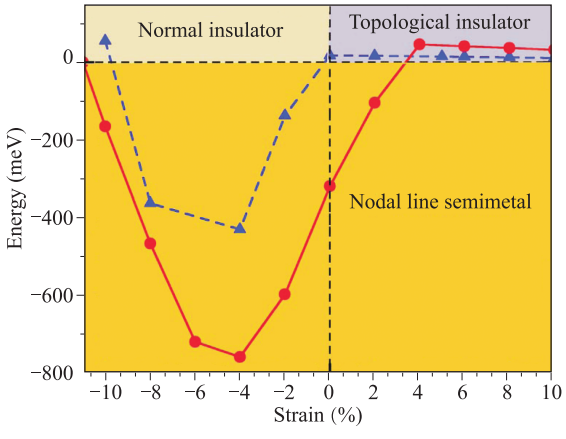

Fig. 7 The calculated direct band gap at the Γ point as a function of lattice strain for Li_2CrN_2 (blue dashed line) and Li_2MoN_2 (solid line).

transition to nodal line semimetal. The topological nodal line semimetal is stable until the strain reaches −9.5%, where Li_2CrN_2 changes into a normal insulator (trivial insulator). As Fig. 7 shows, when the lattice constant $\boldsymbol{a}$ increases, the QSH feature of Li_2CrN_2 survives, although its direct band gap at Γ becomes smaller. The evolution of the band gap of the Li_2MoN_2 at the Γ point indicates that Li_2MoN_2 nanosheet is a nodal line semimetal within the strain range of −11%–3.5%. When the lattice constant is increased by more than 3.5%, Li_2MoN_2 becomes a QSH system. Therefore, the nontrivial topological character of Li_2XN_2 nanolayers is stable over a large strain range, making them highly adaptable in various pressure environments.

5 Summary and conclusions

In this work, based on density-functional theory (DFT) and a $\boldsymbol{K}\cdot\boldsymbol{p}$ effective analysis, we report the existence of a topological nodal line semimetal in Li_2XN_2 (X = Mo, W) nanosheets which crystallizes in the hexagonal space group P6/m. Our calculations show that the band inversion happens between X-d_z^2 (X = Mo, W) and N-p orbitals stemming from a crystal field effect in the nanosheet. The nodal ring is under the protection of reflection symmetry. The large energy range for the linear dispersion of the bands involved in the crossings makes Li_2XN_2 (X = Mo, W) nanosheets an ideal platform to study Dirac and Weyl physics as well as for device design based on 2D topological semimetals. Our calculations show that the topmost valence band and the lowest conduction band of Li_2CrN_2 touch at the Fermi level, making a Dirac coneat the Γ point. In the presence of SOC Li_2CrN_2 hosts QSH states with an energy gap of 17.5 meV.

Electronic supplementary material Supplementary material is available in the online version of this article at https://doi.org/10.1007/s11467-018-0815-x and is accessible for authorized users.

References and notes

1. M. Z. Hasan and C. L. Kane, Topological insulators, *Rev. Mod. Phys.* 82(4), 3045 (2010)
2. K. He, Topological insulator: Both two- and three-dimensional, *Front. Phys.* 7(2), 148 (2012)
3. D. Hsieh, D. Qian, L. Wray, Y. Xia, Y. S. Hor, R. J. Cava, and M. Z. Hasan, A topological Dirac insulator in a quantum spin Hall phase, *Nature* 452(7190), 970 (2008)
4. Y. Xia, D. Qian, D. Hsieh, L. Wray, A. Pal, H. Lin, A. Bansil, D. Grauer, Y. S. Hor, R. J. Cava, and M. Z. Hasan, Observation of a large-gap topological-insulator class with a single Dirac cone on the surface, *Nat. Phys.* 5(6), 398 (2009)
5. S. Y. Xu, C. Liu, N. Alidoust, M. Neupane, D. Qian, I. Belopolski, J. D. Denlinger, Y. J. Wang, H. Lin, L. A. Wray, G. Landolt, B. Slomski, J. H. Dil, A. Marcinkova, E. Morosan, Q. Gibson, R. Sankar, F. C. Chou, R. J. Cava, A. Bansil, and M. Z. Hasan, Observation of a topological crystalline insulator phase and topological phase transition in $Pb_{1-x}Sn_xTe$, *Nat. Commun.* 3(1), 1192 (2012)
6. S. Y. Xu, C. Liu, S. K. Kushwaha, R. Sankar, J. W. Krizan, I. Belopolski, M. Neupane, G. Bian, N. Alidoust, T. R. Chang, H. T. Jeng, C. Y. Huang, W. F. Tsai, H. Lin, F. Chou, P. P. Shibayev, R. J. Cava, and M. Z. Hasan, Observation of Fermi arc surface states in a topological metal, *Science* 347(6219), 294 (2015)
7. Z. Wang, H. Weng, Q. Wu, X. Dai, and Z. Fang, Three-dimensional Dirac semimetal and quantum transport in Cd_3As_2, *Phys. Rev. B* 88(12), 125427 (2013)
8. B. Q. Lv, H. M. Weng, B. B. Fu, X. P. Wang, H. Miao, J. Ma, P. Richard, X. C. Huang, L. X. Zhao, G. F. Chen, Z. Fang, X. Dai, T. Qian, and H. Ding, Experimental discovery of Weyl semimetal TaAs, *Phys. Rev. X* 5(3), 031013 (2015)
9. C. K. Chiu and A. P. Schnyder, Classification of reflection-symmetry-protected topological semimetals and nodal superconductors, *Phys. Rev. B* 90(20), 205136 (2014)
10. J. Behrends, J. W. Rhim, S. Liu, A. G. Grushin, and J. H. Bardarson, Nodal-line semimetals from Weyl superlattices, *Phys. Rev. B* 96(24), 245101 (2017)
11. T. Bzdušek, Q. Wu, A. Ruegg, M. Sigrist, and A. A. Soluyanov, Nodal-chain metals, *Nature* 538(7623), 75 (2016)
12. H. Weng, X. Dai, and Z. Fang, Topological semimetals predicted from first-principles calculations, *J. Phys.: Condens. Matter* 28(30), 303001 (2016)
13. B. Bradlyn, J. Cano, Z. Wang, M. G. Vergniory, C. Felser, R. J. Cava, and B. A. Bernevig, Beyond Dirac and Weyl fermions: Unconventional quasiparticles in conventional crystals, *Science* 353(6299), aaf5037 (2016)
14. H. Weng, C. Fang, Z. Fang, and X. Dai, Coexistence of Weyl fermion and massless triply degenerate nodal points, *Phys. Rev. B* 94(16), 165201 (2016)
15. G. T. Volovik, Momentum space topology of fermion zero modes brane, *JETP Lett.* 75(2), 55 (2002)
16. S. M. Young, S. Zaheer, J. C. Y. Teo, C. L. Kane, E. J. Mele, and A. M. Rappe, Dirac semimetal in three dimensions, *Phys. Rev. Lett.* 108(14), 140405 (2012)
17. M. Dadsetani and A. Ebrahimian, Breaking inversion symmetry induces excitonic peak in optical absorption of topological semimetal, *J. Phys. Chem. Solids* 100, 161 (2017)

18. M. Dadsetani and A. Ebrahimian, Optical distinctions between Weyl semimetal TaAs and Dirac semimetal Na_3Bi: An ab initio investigation, Journal of Elec., *Materi.* 45, 5867 (2016)

19. Z. Wang, Y. Sun, X. Q. Chen, C. Franchini, G. Xu, H. Weng, X. Dai, and Z. Fang, Dirac semimetal and topological phase transitions in A_3Bi (A = Na, K, Rb), *Phys. Rev. B* 85(19), 195320 (2012)

20. A. A. Burkov, Topological semimetals, *Nat. Mater.* 15(11), 1145 (2016)

21. X. Wan, A. M. Turner, A. Vishwanath, and S. Y. Savrasov, Topological semimetal and Fermi arc surface states in the electronic structure of pyrochlore iridates, *Phys. Rev. B* 83(20), 205101 (2011)

22. A. A. Burkov, M. D. Hook, and L. Balents, Topological nodal semimetals, *Phys. Rev. B* 84(23), 235126 (2011)

23. M. Z. Hasan, S. Y. Xu, I. Belopolski, and S. M. Huang, Discovery of weyl fermion semimetals and topological fermi arc states, *Annu. Rev. Condens. Matter Phys.* 8(1), 289 (2017)

24. C. Fang, Y. Chen, H. Y. Kee, and L. Fu, Topological nodal line semimetals with and without spin-orbital coupling, *Phys. Rev. B* 92(8), 081201 (2015)

25. Y. X. Zhao, A. P. Schnyder, and Z. D. Wang, Unified theory of PT and CP invariant topological metals and nodal superconductors, *Phys. Rev. Lett.* 116(15), 156402 (2016)

26. R. Yu, Z. Fang, X. Dai, and H. Weng, Topological nodal line semimetals predicted from first-principles calculations, *Front. Phys.* 12(3), 127202 (2017)

27. H. Weng, C. Fang, Z. Fang, B. A. Bernevig, and X. Dai, Weyl semimetal phase in noncentro-symmetric transition-metal monophosphides, *Phys. Rev. X* 5(1), 011029 (2015)

28. Q. D. Gibson, L. M. Schoop, L. Muechler, L. S. Xie, M. Hirschberger, N. P. Ong, R. Car, and R. J. Cava, Three-dimensional Dirac semimetals: Design principles and predictions of new materials, *Phys. Rev. B* 91(20), 205128 (2015)

29. M. Neupane, S. Y. Xu, R. Sankar, N. Alidoust, G. Bian, C. Liu, I. Belopolski, T. R. Chang, H. T. Jeng, H. Lin, A. Bansil, F. Chou, and M. Z. Hasan, Observation of a three-dimensional topological Dirac semimetal phase in high-mobility Cd_3As_2, *Nat. Commun.* 5(1), 3786 (2014)

30. S. Borisenko, Q. Gibson, D. Evtushinsky, V. Zabolotnyy, B. Büchner, and R. J. Cava, experimental realization of a three-dimensional Dirac semimetal, *Phys. Rev. Lett.* 113(2), 027603 (2014)

31. Z. K. Liu, B. Zhou, Y. Zhang, Z. J. Wang, H. M. Weng, D. Prabhakaran, S.-K. Mo, Z. X. Shen, Z. Fang, X. Dai, Z. Hussain, and Y. L. Chen, Discovery of a three-dimensional topological Dirac semimetal, Na_3Bi, *Science* 343(6173), 864 (2014)

32. S. Y. Xu, C. Liu, S. K. Kushwaha, R. Sankar, J. W. Krizan, I. Belopolski, M. Neupane, G. Bian, N. Alidoust, T. R. Chang, H. T. Jeng, C. Y. Huang, W. F. Tsai, H. Lin, P. P. Shibayev, F. C. Chou, R. J. Cava, and M. Z. Hasan, Observation of Fermi arc surface states in a topological metal, *Science* 347(6219), 294 (2015)

33. G. Bian, T. R. Chang, R. Sankar, S. Y. Xu, H. Zheng, T. Neupert, C. K. Chiu, S. M. Huang, G. Chang, I. Belopolski, D. S. Sanchez, M. Neupane, N. Alidoust, C. Liu, B. Wang, C. C. Lee, H. T. Jeng, C. Zhang, Z. Yuan, S. Jia, A. Bansil, F. Chou, H. Lin, and M. Z. Hasan, Topological nodal-line fermions in spin-orbit metal $PbTaSe_2$, *Nat. Commun.* 7, 10556 (2016)

34. Y. Wu, L. L. Wang, E. Mun, D. D. Johnson, D. Mou, L. Huang, Y. Lee, S. L. Bud'ko, P. C. Canfield, and A. Kaminski, Dirac node arcs in $PtSn_4$, *Nat. Phys.* 12(7), 667 (2016)

35. L. M. Schoop, M. N. Ali, C. Straßer, A. Topp, A. Varykhalov, D. Marchenko, V. Duppel, S. S. P. Parkin, B. V. Lotsch, and C. R. Ast, Dirac cone protected by non-symmorphic symmetry and three-dimensional Dirac line node in ZrSiS, *Nat. Commun.* 7, 11696 (2016)

36. M. Neupane, I. Belopolski, M. M. Hosen, D. S. Sanchez, R. Sankar, M. Szlawska, S. Y. Xu, K. Dimitri, N. Dhakal, P. Maldonado, P. M. Oppeneer, D. Kaczorowski, F. Chou, M. Z. Hasan, and T. Durakiewicz, Observation of topological nodal fermion semimetal phase in ZrSiS, *Phys. Rev. B* 93(20), 201104 (2016)

37. T. Liang, Q. Gibson, M. N. Ali, M. Liu, R. J. Cava, and N. P. Ong, Ultrahigh mobility and giant magnetoresistance in the Dirac semimetal Cd3As2, *Nat. Mater.* 14(3), 280 (2015)

38. Y. Zhao, H. Liu, C. Zhang, H. Wang, J. Wang, Z. Lin, Y. Xing, H. Lu, J. Liu, Y. Wang, S. M. Brombosz, Z. Xiao, S. Jia, X. C. Xie, and J. Wang, Anisotropic Fermi surface and quantum limit transport in high mobility three-dimensional Dirac semimetal Cd_3As_2, *Phys. Rev. X* 5(3), 031037 (2015)

39. H. Wang, H. Wang, H. Liu, H. Lu, W. Yang, S. Jia, X.J. Liu, X. C. Xie, J. Wei, and J. Wang, Observation of superconductivity induced by a point contact on 3D Dirac semimetal Cd_3As_2 crystals, *Nat. Mater.* 15(1), 38 (2016)

40. H. Weng, Y. Liang, Q. Xu, R. Yu, Z. Fang, X. Dai, and Y. Kawazoe, Topological node-line semimetal in three-dimensional graphene networks, *Phys. Rev. B* 92(4), 045108 (2015)

41. R. Yu, H. Weng, Z. Fang, X. Dai, and X. Hu, Topological node-line semimetal and Dirac semimetal state in antiperovskite Cu_3PdN, *Phys. Rev. Lett.* 115(3), 036807 (2015)

42. Y. Kim, B. J. Wieder, C. L. Kane, and A. M. Rappe, Dirac line nodes in inversion-symmetric crystals, *Phys. Rev. Lett.* 115(3), 036806 (2015)

43. J. Zhang, M. Gao, J. Zhang, X. Wang, X. Zhang, M. Zhang, W. Niu, R. Zhang, and Y. Xu, Transport evidence of 3D topological nodal-line semimetal phase in ZrSiS, *Front. Phys.* 13(1), 137201 (2018)
44. L. M. Schoop, M. N. Ali, C. Straßer, A. Topp, A. Varykhalov, D. Marchenko, V. Duppel, S. S. P. Parkin, B. V. Lotsch, and C. R. Ast, Dirac cone protected by non-symmorphic symmetry and three-dimensional Dirac line node in ZrSiS, *Nat. Commun.* 7, 11696 (2016)
45. S. M. Young and C. L. Kane, Dirac semimetals in two dimensions, *Phys. Rev. Lett.* 115(12), 126803 (2015)
46. C. Niu, P. M. Buhl, G. Bihlmayer, D. Wortmann, Y. Dai, S. Blügel, and Y. Mokrousov, Two-dimensional topological nodal line semimetal in layered X_2Y (X = Ca, Sr, and Ba; Y=As, Sb, and Bi), *Phys. Rev. B* 95(23), 235138 (2017)
47. J. L. Lu, W. Luo, X. Y. Li, S. Q. Yang, J. X. Cao, X. G. Gong, and H. J. Xiang, Two-dimensional node-line semimetals in a honeycomb-Kagome lattice, *Chin. Phys. Lett.* 34(5), 057302 (2017)
48. Y. J. Jin, R. Wang, J. Z. Zhao, Y. P. Du, C. D. Zheng, L. Y. Gan, J. F. Liu, H. Xu, and S. Y. Tong, The prediction of a family group of two-dimensional node-line semimetals, *Nanoscale* 9(35), 13112 (2017)
49. B. Yang, X. Zhang, and M. Zhao, Dirac node lines in two-dimensional Lieb lattices, *Nanoscale* 9(25), 8740 (2017)
50. A. Ebrahimian and M. Dadsetani, Dependence of topological and optical properties on surface-terminated groups in two-dimensional molybdenum dinitride and tungsten dinitride nanosheets, *Phys. Chem. Chem. Phys.* 19(45), 30301 (2017)
51. B. Feng, B. Fu, S. Kasamatsu, S. Ito, P. Cheng, C. C. Liu, Y. Feng, S. Wu, S. K. Mahatha, P. Sheverdyaeva, P. Moras, M. Arita, O. Sugino, T. C. Chiang, K. Shimada, K. Miyamoto, T. Okuda, K. Wu, L. Chen, Y. Yao, and I. Matsuda, Experimental realization of two-dimensional Dirac nodal line fermions in monolayer Cu_2Si, *Nat. Commun.* 8(1), 1007 (2017)
52. N. B. Kopnin, T. T. Heikkila, and G. E. Volovik, High temperature surface superconductivity in topological flat-band systems, *Phys. Rev. B* 83(22), 220503 (2011)
53. Z. Y. Zhu, Y. C. Cheng, and U. Schwingenschlögl, Giant spin-orbit-induced spin splitting in two-dimensional transition-metal dichalcogenide semiconductors, *Phys. Rev. B* 84(15), 153402 (2011)
54. D. Xiao, G. B. Liu, W. Feng, X. Xu, and W. Yao, Coupled spin and valley physics in monolayers of MoS_2 and other group-VI Dichalcogenides, *Phys. Rev. Lett.* 108(19), 196802 (2012)
55. Y. Ma, L. Kou, X. Li, Y. Dai, and T. Heine, Two-dimensional transition metal dichalcogenides with a hexagonal lattice: Room-temperature quantum spin Hall insulators, *Phys. Rev. B* 93(3), 035442 (2016)
56. P. F. Liu, L. Zhou, T. Frauenheim, and L. M. Wu, New quantum spin Hall insulator in two-dimensional MoS_2, with periodically distributed pores, *Nanoscale* 8(9), 4915 (2016)
57. P. F. Liu, L. Zhou, T. Frauenheim, and L. M. Wu, Two dimensional hydrogenated molybdenum and tungsten dinitrides MN_2H_2 (M = Mo, W) as novel quantum spin hall insulators with high stability, *Nanoscale* 9(3), 1007 (2017)
58. N. Alidoust, G. Bian, S. Y. Xu, R. Sankar, M. Neupane, C. Liu, I. Belopolski, D. X. Qu, J. D. Denlinger, F. C. Chou, and M. Z. Hasan, Observation of monolayer valence band spin-orbit effect and induced quantum well states in MoX_2, *Nat. Commun.* 5(1), 4673 (2014)
59. K. Dolui, I. Rungger, C. Das Pemmaraju, and S. Sanvito, Possible doping strategies for MoS_2 monolayers: An ab initio study, *Phys. Rev. B* 88(7), 075420 (2013)
60. J. Heyd, G. E. Scuseria, and M. Ernzerhof, Hybrid functionals based on a screened Coulomb potential, *J. Chem. Phys.* 118(18), 8207 (2003)
61. K. Hummer, J. Harl, and G. Kresse, Heyd-Scuseria-Ernzerhof hybrid functional for calculating the lattice dynamics of semiconductors, *Phys. Rev. B* 80(11), 115205 (2009)
62. F. Tran and P. Blaha, Accurate band gaps of semiconductors and insulators with a semilocal exchange-correlation potential, *Phys. Rev. Lett.* 102(22), 226401 (2009)
63. P. Blaha, K. Schwarz, G. Madsen, D. Kvasicka, and J. Luitz, WIEN2k, An Augmented Plane Wave Plus Local OrbitalsProgram for Calculating Crystal Properties, TU Vienna, Vienna, 2001
64. V. Blum, R. Gehrke, F. Hanke, P. Havu, V. Havu, X. Ren, K. Reuter, and M. Scheffler, Ab initio molecular simulations with numeric atom-centered orbitals, *Comput. Phys. Commun.* 180(11), 2175 (2009)
65. J. P. Perdew, K. Burke, and M. Ernzerhof, Generalized gradient approximation made simple, *Phys. Rev. Lett.* 77(18), 3865 (1996)
66. X. Zhang, X. F. Qiao, W. Shi, J. B. Wu, D. S. Jiang, and P. H. Tan, Phonon and Raman scattering of two-dimensional transition metal dichalcogenides from monolayer, multilayer to bulk material, *Chem. Soc. Rev.* 44(9), 2757 (2015)
67. See the Supplemental Material.
68. G. Bian, T. R. Chang, H. Zheng, S. Velury, S. Y. Xu, T. Neupert, C. K. Chiu, S. M. Huang, D. S. Sanchez, I. Belopolski, N. Alidoust, P. J. Chen, G. Chang, A. Bansil, H. T. Jeng, H. Lin, and M. Z. Hasan, Drumhead surface states and topological nodal-line fermions in $TlTaSe_2$, *Phys. Rev. B* 93(12), 121113 (2016)
69. L. Fu, C. L. Kane, and E. J. Mele, Topological insulators in three dimensions, *Phys. Rev. Lett.* 98(10), 106803 (2007)
70. L. Fu and C. L. Kane, Topological insulators with inversion symmetry, *Phys. Rev. B* 76(4), 045302 (2007)